Lab on a Chip

PAPER

View Article Online
View Journal | View Issue

Cite this: *Lab Chip*, 2025, **25**, 6662

Multiscale microfluidic platform with vacuum-driven chambers for automated high-volume ssDNA generation

Anni Hu,[a] Yang Bu,[b] Yuze Liu,[a] Yung Ching Lee,[b] Sheng Ni[b] and Levent Yobas*[ab]

We present a multiscale microfluidic platform for automated high-volume single-stranded DNA (ssDNA) generation through plasmonic bead-based PCR. Central to the system are vacuum-driven chambers capable of handling fluid volumes in the tens of microliters—at least an order of magnitude larger than conventional microfluidic chambers. These chambers are seamlessly integrated with microfluidic components such as micromixers and pneumatically actuated microvalves, enabling precise fluidic transport in processing high volumes. This architecture overcomes limitations of pressure-driven flow in exchanging fluids in deep geometries. Direct vacuum access to these chambers improves fluid handling efficiency while reducing hardware complexity. We demonstrate the platform's capabilities through automated ssDNA preparation where plasmonic thermocycling is achieved *via* volumetric heating using gold nanorods dispersed in the reaction mixture. Magnetic beads functionalized with reverse primers facilitate selective amplification and effective strand separation. Despite the large reaction volume (20 μL), 20 PCR cycles are completed within 12 minutes. Fluorescence-based assays confirm 66% recovery of ssDNA from the beads, with 92% retention of complementary strands, indicating minimal contamination by double-stranded DNA (dsDNA). This multiscale integration of vacuum-driven chambers with microfluidic control offers a scalable and automated platform for preparative applications where high-volume processing is essential.

Received 11th August 2025,
Accepted 8th October 2025

DOI: 10.1039/d5lc00785b

rsc.li/loc

1 Introduction

Single-stranded DNA (ssDNA) is commonly used in molecular biology and biotechnology serving as a template in techniques such as pyrosequencing and solid-phase DNA sequencing.[1,2] It is also instrumental in single nucleotide polymorphism and single-strand conformation polymorphism analysis.[3–5] In gene editing, ssDNA acts as a guide template for homologous directed repair within the CRISPR-Cas9 system.[6] In diagnostics and sensors, ssDNA is employed as a capture probe, selectively binding to targets like viral RNA or proteins, thereby enabling efficient and precise biomarker detection and quantification. This specificity significantly enhances the utility of ssDNA in microarrays,[7–9] gene sensors,[10] and biosensors.[11–13] In methods like rolling circle amplification[14,15] and loop-mediated isothermal amplification,[16,17] ssDNA works with nanomaterials to amplify signals. In addition, ssDNA is utilized in fluorescent *in situ* hybridization to locate specific DNA or RNA sequences.[18,19] Furthermore, ssDNA plays a pivotal role in the *in vitro* aptamer selection process, particularly in systematic evolution of ligands by exponential enrichment (SELEX).[20] These ssDNA aptamers can then be applied in diverse fields such as biosensing,[21] targeted drug delivery,[22] and molecular diagnostics.[23] Thus, the generation of high-quality ssDNA is essential for ensuring the accuracy and reliability of these applications.

The most common technique for generating ssDNA, namely heat and cool, involves heating double-stranded DNA (dsDNA) to break the hydrogen bonds that hold the strands together. This is followed by a cooling step to stabilize the dissociated strands. However, this approach suffers from low efficiency and reproducibility.[24] ssDNA can also be generated by selectively digesting unwanted strand of a dsDNA using enzymes such as lambda or T7 exonuclease, leaving behind the desired ssDNA.[25,26] This method is highly dependent on the efficiency of 5′-end phosphorylation of the strand; incomplete degradation of the phosphorylated strand can lead to the accumulation of residual double-stranded DNA in the reaction mixture. This, in turn, can compromise the efficiency of downstream purification steps such as phenol/

[a] *Department of Chemical and Biological Engineering, The Hong Kong University of Science and Technology, Clear Water Bay, Hong Kong, SAR, China.*
E-mail: eelyobas@ust.hk
[b] *Department of Electronic and Computer Engineering, The Hong Kong University of Science and Technology, Clear Water Bay, Hong Kong, SAR, China*

chloroform extraction or PAGE, which are typically required but are limited by their complexity and low separation efficiency.

Another common technique for generating ssDNA involves PCR in the presence of a biotinylated and a non-biotinylated primer. Non-biotinylated ssDNA can then be released by heat or alkaline denaturation from the biotinylated dsDNA amplicons after being captured on streptavidin-coated magnetic beads.[27] Alternatively, non-biotinylated ssDNA can be recovered from urea gels following electrophoresis, after being well separated from the slower-migrating streptavidin-biotinylated–ssDNA complex.[28] However, these approaches face the loss of a large amount of ssDNA. Asymmetric PCR[29] generates ssDNA by using a higher concentration of primer for the target strand. However, this method is rather inefficient and unpredictable. Additionally, it necessitates the isolation of ssDNA from dsDNA that is also produced in the process until the primer of lower concentration is depleted. While these issues can be mitigated by using linear-after-the-exponential (LATE)-PCR,[30,31] this approach deals with intricate optimization of the limiting and excess primer design.

On-bead or bead-based PCR is an effective way of producing ssDNA in various applications, including DNA sequencing,[32,33] pathogen detection,[34,35] and protein screening.[36] As a variant of PCR, this method involves the immobilization of primers on beads, facilitating the amplification of multiple copies of DNA template that are tethered to these beads. Shendure *et al.* achieved efficient and high-precision genome sequencing by amplifying DNA polymers (called polonies) on beads.[32] McEvoy and colleagues used the method to enhance the output of pre-captured libraries for next-generation sequencing.[33] Lermo *et al.* enhanced the detection sensitivity and speed of pathogenic genomes.[34] Hilton *et al.* developed a microfluidic platform that integrates bead-based PCR for the rapid detection of *Bordetella pertussis* DNA.[35] Kojima *et al.* used it for enabling efficient screening of transcription factor target genes.[36]

While PCR, especially bead-based PCR can be employed to generate ssDNA, the process typically requires several hours due to slow thermocycling. Additionally, contaminations arising from the manual operations including sampling, separation, elution, and collection may lead to poor results. Thermocycling can be accelerated to just minutes when performed on a microfluidic chip. This approach also offers automation and integration with other components. Numerous demonstrations have showcased various chips and strategies for thermocycling, ranging from Joule heating to radiative heating, with plasmonic photothermal heating emerging as the most recent innovation. Plasmonic photothermal heating leverages surface plasmon resonance in irradiated noble metals. Initially applied to PCR using gold nanoparticles in glass tubes,[37] later adaptations for chip-scale demonstrations have shifted to gold metal films.[38] This shift has resulted in the loss of key advantages offered by nanoparticles, such as simplified chip fabrication and extremely rapid PCR, despite accommodating larger sample volumes. The surface heating provided by metal films as opposed to the bulk heating from nanoparticles limits the chamber volume to ensure the temperature uniformity. While a small chamber is beneficial for analytical applications—where minimizing sample and reagent volumes reduces costs—it poses challenges for preparative applications that require high throughput for downstream use, such as the generation of ssDNA.

Here, we present the concept of vacuum-driven chambers integrated into a microfluidic platform to enable the handling of increased fluid volumes through microchannels. This approach leverages the automation and precision of microfluidics while overcoming the volume constraints typical of conventional systems. Additionally, it cuts down the number of pumps required to deliver multiple samples and reagents through microchannels. Performing PCR in these chambers effectively bypasses air bubbles observed during thermocycling. The utility of the concept is showcased on the generation of ssDNA using plasmonic bead-based PCR enabled by gold nanorods (AuNRs). Given high volume capacity of vacuum-driven chambers, AuNRs are particularly well-suited for enabling uniform volumetric heating across tens of microliters, thereby overcoming the thermal limitations of surface-heated thin films. Additionally, AuNRs, compared to other plasmonic nanoparticles offer superior photothermal conversion efficiency due to their high absorption-to-extinction ratio, tuneable longitudinal plasmon resonance in the near-infrared region, and favourable aspect ratio, which collectively enable efficient volumetric heating.[39–41]

2 System

Fig. 1a illustrates the fluidic layout of the system featuring three vacuum-driven chambers alongside six vacuum-activated microvalves for fluidic control and automation. The layout includes a spiral micromixer to effectively mix ssDNA template and master mix containing forward primers and AuNRs as they are transported from respective reservoirs into a vacuum-driven chamber designated for PCR. The remaining two vacuum-driven chambers are designated for collecting ssDNA amplicons and waste. The layout also includes additional reservoirs for sourcing magnetic beads and elution buffer containing AuNRs, which are used to enable plasmonic heating for thermal denaturation of dsDNA amplicons.

The system consists of four layers as illustrated in Fig. 1a, all defined in polydimethylsiloxane (PDMS): (1) A fluidic layer with microchannels for transporting liquids; (2) a membrane layer that deforms under pneumatic pressure to activate the microvalves that are normally closed; (3) a pneumatic layer with through-holes defining the reservoirs as well as vacuum-driven chambers along with microchannels that deliver suction to activate the microvalves; and (4) a capping layer that encloses the chambers and incorporates microchannels for applying either vacuum or atmospheric pressure to drive fluid movement in or out of the chambers. The capping layer also contains through-holes that contribute the reservoir structures.

The system operation involves: (1) loading the PCR chamber, (2) introducing magnetic beads, (3) performing plasmonic PCR, (4) removing waste and executing purification washes, and (5)

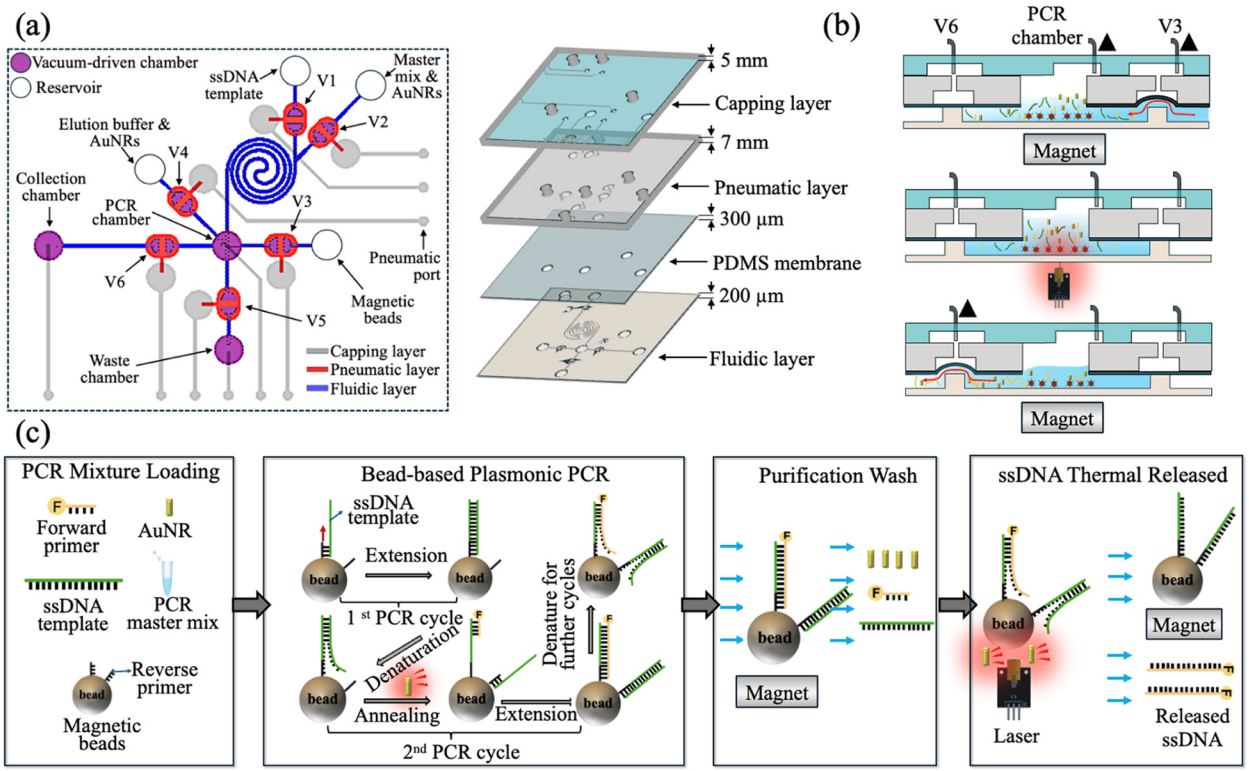

Fig. 1 Schematics describing (a) microfluidic system for high-throughput generation of ssDNA, (b) system operation key steps and (c) plasmonic bead-based PCR implemented within the system. (a) System fluidic layout and exploded view of the structure. (b) Cross-sectional illustrations describing key steps: (i) the loading of magnetic beads into the vacuum-driven PCR chamber after the loading of a mixture of ssDNA template and master mix containing AuNRs; (ii) pulsed laser irradiation of the chamber from below during bead-based plasmonic PCR; (iii) the elution and collection of amplified ssDNA after the removal of the waste by a purification wash and then the thermal (plasmonic) denaturation release of ssDNA. The arrowheads next the pneumatic ports point at the suction direction while their absence indicates the application of atmospheric pressure. (c) Illustrations describing first and second cycles of plasmonic bead-based PCR and subsequent purification wash and plasmonic thermal release of ssDNA.

thermally eluting ssDNA. The entire process is programmable and fully automated, including the coordinated control of the vacuum-driven chambers and microvalves, laser source, cooling fan, and magnet drive. It begins with the application of vacuum to the PCR chamber to load a mixture of ssDNA template and master mix that also contains AuNRs along with forward primers, while activating microvalves V1 and V2. Applying the vacuum to the PCR chamber, magnetic beads immobilized with reverse primers are then introduced by activating microvalve V3. Subsequently, plasmonic bead-based PCR is performed by alternatingly pulsing a laser irradiating the chamber from below and a cooling fan directed at the chamber side. This leads to the accumulation of dsDNA amplicons on the beads. A strong magnet is held near the chamber to immobilize the beads during cleanup and elution. The chamber contents, excluding the beads, are removed by applying vacuum to the waste chamber with microvalve V5 activated. Subsequently, the beads are washed three times using an elution buffer containing AuNRs. Each wash cycle involves applying vacuum to the PCR chamber with microvalve V4 activated to fill it with the buffer, followed by applying vacuum to the waste chamber to evacuate the buffer with microvalve V5 activated. Finally, a brief laser pulse is applied for plasmonic heating, thermally denaturing the bead-bound duplexes and releasing ssDNA into solution. The released ssDNA is then eluted into the collection chamber by activating microvalve V6. The core steps of this automated workflow—including bead loading, plasmonic PCR, and thermal elution—are schematically illustrated in Fig. 1b.

Plasmonic bead-based PCR and the subsequent thermal denaturation of dsDNA amplicons are described in Fig. 1c. Reverse primers with biotinylated 5′ ends are immobilized on streptavidin-coated magnetic beads. In the initial thermal cycle, these primers anneal to ssDNA templates and are extended to form complementary strands. In subsequent cycles, the ssDNA templates are released and re-anneal to fresh reverse primers, while forward primers bind to the complementary strands and are extended, amplifying the ssDNA templates. This cyclic process results in the accumulation of dsDNA amplicons tethered to the beads *via* the reverse primers. Upon plasmonic heating, thermal denaturation releases the ssDNA strands, which are then collected for downstream applications.

3 Theory

The PCR chamber temperature reaches a steady-state value, T_{ss}, as the rate of heat input, Q_{in}, due to the laser irradiation balances the rate of heat loss, Q_{ext}, to the exterior at a constant ambient temperature of T_{amb}. Under steady-state

conditions, the chamber is assumed to exhibit a uniform temperature distribution.

The rate of heat input due to the laser irradiation of the chamber content containing AuNRs can be expressed as:

$$Q_{\text{in}} = I(1 - 10^{-A_\lambda})\eta \quad (1)$$

where I is the incident laser power, η the photothermal conversion efficiency, and A_λ the solution absorbance at the laser wavelength λ (808 nm) according to Beer–Lambert's Law.

The rate of heat loss primarily through thermal conduction and convection can be expressed as:

$$Q_{\text{ext}} = US_{\text{eff}}(T_{\text{ss}} - T_{\text{amb}}) \quad (2)$$

where U is the overall thermal conductance and S_{eff} the effective heat transfer area.

The thermal behaviour of the chamber is governed by the heat balance equation:

$$\sum_i m_i c_{\text{p},i} \frac{\mathrm{d}T}{\mathrm{d}t} = Q_{\text{in}} - Q_{\text{ext}} \quad (3)$$

where m_i and $c_{\text{p},i}$ are the mass and specific heat capacity of the chamber elements, mainly including the liquid and the chamber wall segments over which thermal conduction takes place, T the temperature, and t time.

At steady state, temperature is constant and Q_{in} and Q_{ext} balance each other. Rearranging the equations yields an expression for the photothermal conversion efficiency:

$$\eta = \frac{US_{\text{eff}}(T_{\text{ss}} - T_{\text{amb}})}{I(1 - 10^{-A_\lambda})} \quad (4)$$

Here, the only unknown is the product US_{eff}, but can be determined from cooling dynamics (the measured cooling time constant) as described below.

During the cooling phase, the laser is turned off, so there is no external energy input ($Q_{\text{in}} = 0$). Eqn (3) simplifies to:

$$\sum_i m_i c_{\text{p},i} \frac{\mathrm{d}T}{\mathrm{d}t} = -US_{\text{eff}}(T_{\text{ss}} - T_{\text{amb}}) \quad (5)$$

Integrating both sides of eqn (5) yields an exponential decay in temperature over time, characterized by a time constant of τ_{s}. This constant can be extracted from the slope of a linear fit of t *versus* $-\ln(\theta)$, where θ is the measured temperature T over time t, normalized according to:

$$\theta = \frac{T - T_{\text{amb}}}{T_{\text{ss}} - T_{\text{amb}}} \quad (6)$$

Using τ_{s}, the product term can be calculated as:

$$US_{\text{eff}} = \frac{\sum_i m_i c_{\text{p},i}}{\tau_{\text{s}}} \quad (7)$$

Substituting this into eqn (4) allows for the determination of the photothermal conversion efficiency η.

4 Methods

Reagents and materials

FAM-labelled forward primer, biotin-labelled reverse primer as well as 80 nt ssDNA template were synthesized by Integrated DNA Technologies (Coralville, IA), respectively, as (5′-FAM-GGAACTACATGAGAGTAAGC-3′), (5′-biotin-CTACCT ACGATCTGA CTAGC-3′), and (5′-CTACCTACGATCTGACTAG CGATGTAGGCCAT CCTGTGGGGGTACGGGGCGGGCTGTG GTGCTTACTCTCATGTAGTTCC-3′). Streptavidin-coated 2.8 μm magnetic beads were purchased from Invitrogen (Carlsbad, CA). KOD One™ PCR Master Mix, containing KOD polymerase, dNTPs, and Mg^{2+}, was obtained from TOYOBO (Osaka, Japan). PCR polymer functionalized AuNRs (PCR-808-DIH-50-1) with dimensions of 10 nm in diameter and 41 nm in length were sourced from Nanopartz (Loveland, CO). The binding buffer for bead functionalization consisted of 10 mM Tris–HCl (pH 7.5), 1 mM EDTA, and 2 M NaCl, purchased from Sigma-Aldrich (St. Louis, MO). Elution buffers included ultrapure distilled water (Thermo Fisher Scientific, Waltham, MA), 10 mM Tris–HCl (pH 8.0; Sangon Biotech, Shanghai, China), 2.5 mM Tris–HCl (pH 7.5; Thermo Fisher Scientific), or TGK buffer, which consisted of 125 mM Tris–HCl, 960 mM glycine (Sigma-Aldrich), and 25 mM KH_2PO_4 (Avantor, Radnor, PA), adjusted to pH 8.3. The PDMS membrane (300 μm thick) was sourced from Westru (Hangzhou, China). Agarose and SYBR™ Safe DNA Gel Stain were purchased from Invitrogen, while the DNA loading buffer was obtained from Yeasen (Shanghai, China). PDMS was obtained from Dow Corning (Sylgard 184, Midland, MI).

Hardware

A set of solenoid valves (LHDA0533115H, The LEE Company, Westbrook, CT) supplied from a mini pump (CJWP08-AB03A10, Conjoin, Xiamen, China) was used to control fluidic transport by switching pneumatic lines between atmospheric pressure and vacuum. Thermal cycling relied on alternating plasmonic heating *via* 808 nm laser illumination at 0.28 W mm^{-2} (Arm Laser, Shenzhen, China) and forced convection *via* a cooling fan (AFB0512MA, Delta Electronics, Taipei, Taiwan). Plasmonic heating was also used for thermal elution of ssDNA from beads. Temperature was monitored and calibrated with a K-type thermocouple (Omega Engineering, Norwalk, CT) immersed in the reaction mixture. An SG90 micro servo (TowerPro, Taipei) with a 180° rotation range was controlled by program to manipulate the magnet, thereby immobilizing the magnetic beads for the ssDNA elution steps. All hardware components were managed by a microcontroller board (Arduino Mega, Ivrea, Italy), which implemented a custom PID control algorithm for heater regulation based on thermocouple feedback (Fig. S1).

Simulations

Transient thermal simulations were conducted using COMSOL Multiphysics v6.3 (COMSOL Inc., Burlington, MA) on a three-dimensional model illustrated in Fig. S2 The system time constant, derived from a cooling experiment (Fig. S3), was used to calculate the photothermal conversion efficiency. The convective heat transfer coefficient during forced cooling was determined using equations provided in the SI. Parameters and material properties used are listed in Tables S1 and S2.

Fabrication

The system was fabricated based on multilayer soft lithography with key process steps illustrated in Fig. S4. Templates for the fluidic, pneumatic, and capping layers were patterned on 4 inch silicon wafers *via* UV photolithography and dry etching. The fluidic and pneumatic layers contained 60 μm-deep channels while the capping layer incorporated channels with a depth of 100 μm. To facilitate PDMS release, the wafers were silanized overnight using chlorotrimethylsilane. PDMS base and curing agent were mixed at a 10 : 1 ratio and then degassed to eliminate bubbles. For the fluidic layer, the mixture was spin-coated onto the template at 500 rpm for 25 s to achieve a thickness of approximately 200 μm, followed by curing at 120 °C for 10 min. For the pneumatic and capping layers, the mixture was poured directly onto their respective templates, with volumes adjusted to yield final thicknesses of 7 mm and 5 mm, respectively. After curing, the layers were carefully peeled off from the templates. Reservoir and pneumatic port holes were then punched into the pneumatic and capping layers using 3 mm- and 1 mm-diameter punchers, respectively. The pneumatic and fluidic layers were then aligned and bonded using oxygen plasma surface activation, with a 300 μm-thick PDMS membrane sandwiched in between, followed by baking at 120 °C for 10 min to enhance the bonding strength. Finally, the capping layer was aligned and placed atop the pneumatic layer without permanent bonding to complete the multilayer structure.

Magnetic beads

A 50 μL aliquot of streptavidin-coated magnetic beads were taken from the stock, and the supernatant was removed. The beads were washed three times with deionized water and then resuspended in 50 μL of binding buffer (10 mM Tris–HCl, pH 7.5, 1 mM EDTA, 2 M NaCl) containing 2 μL of 100 μM biotinylated reverse primer. The suspension was incubated overnight to allow immobilization of the primer onto the bead surface for subsequent amplification.

Bead-based plasmonic PCR

Bead-based plasmonic PCR was performed in a partially filled reaction chamber with a diameter of 3 mm and a total height of 7 mm, containing a 3.0 mm-high column of PCR mixture topped by an air phase. The mixture included: 10 μL of 2× KOD One™ PCR Master Mix, 0.6 μL of 100 μM forward primer, 5 μL of ssDNA template, 0.9 μL of 60 nM AuNRs, and 60 μg of primer-functionalized magnetic beads. The system was mounted on a 3D-printed stage, ensuring precise alignment between the PCR chamber and laser beam with a spot diameter of approximately 3 mm directed at the chamber bottom. The fan was positioned on the stage to deliver directed airflow during the cooling phase. Real-time temperature monitoring was achieved using the thermocouple inserted into the PCR mixture. Each thermal cycle consisted of denaturation at 90 °C followed by annealing and extension at 47 °C, repeated for 20 cycles.

During the wash and elution steps, a strong magnet was placed adjacent to the PCR chamber to immobilize the magnetic beads. Initially, the reaction mixture was removed by applying vacuum to the waste chamber while activating valve V5. The wash step involved introducing elution buffer containing 2.5 nM AuNRs into the PCR chamber by applying vacuum while activating valve V4, followed by removal into the waste chamber through valve V5. This wash cycle was repeated three times. After washing, the PCR chamber was filled with a 6 μL of elution buffer. Thermal elution of ssDNA was then performed *via* plasmonic heating, followed by transferring the released ssDNA in the elution buffer into the collection chamber by applying vacuum while activating valve V6.

ssDNA analysis and validation

Eluted ssDNA products were analyzed by 3% agarose gel electrophoresis run at 110 V for 35 min to evaluate elution efficiency. A 10 μM stock solution of 80 bp ssDNA was used as a size marker. Concentration and purity were measured using a NanoDrop microvolume spectrophotometer (Thermo Fisher Scientific) *via* UV-vis absorbance at 260 nm.

Validation of ssDNA release was performed *via* fluorescence imaging of beads under identical microscope settings using an epi-fluorescence microscope equipped with a 50× objective lens (Nikon, Tokyo, Japan). Fluorescence intensities were quantified using ImageJ software (NIH). Following on-chip amplification, beads were collected into an Eppendorf tube and washed three times with ultrapure water to remove residual reagents. Imaging at this stage established the baseline fluorescence signal. Beads were then reintroduced into the PCR chamber for thermal elution at 80 °C for 40 s in 10 mM Tris–HCl buffer (pH 8.0). Post-elution imaging was conducted to evaluate residual fluorescence, indicating ssDNA release efficiency. To further confirm the presence of complementary strands, the same beads were incubated for 2 h at room temperature in an Eppendorf tube containing 2 μL of 100 μM fluorescently labelled forward primers and 8 μL of 35 mM $MgCl_2$. Following three wash cycles with ultrapure water, fluorescence imaging was performed to assess hybridization, confirming whether the eluted products were predominantly single-stranded. Additionally, a fresh batch of 60 μg beads functionalized with reverse primers was incubated for 12 h at room temperature with the eluted products in a 10 μL mixture containing $MgCl_2$.

After washing cycles, fluorescence imaging and analysis were performed under identical conditions.

ssDNA quantification

A calibration curve was established to correlate fluorescence intensity with ssDNA concentration. ssDNA solutions ranging from 0.01 μM to 50 μM were prepared in 10 μL reaction volumes containing 35 mM $MgCl_2$ and mixed with 60 μg of beads functionalized with reverse primers in Eppendorf tubes. The mixtures were incubated at room temperature for 1 h. Following incubation, the beads were washed three times with ultrapure water to remove unbound ssDNA. Fluorescence imaging was performed on the beads, and the images were analyzed using ImageJ software (NIH) to quantify fluorescence intensity. All measurements were performed in triplicate. A logistic function was fitted to the full concentration range (0.01–50 μM), while a linear regression model was applied to the low-concentration range (0–1 μM) to enhance sensitivity. The resulting calibration curve was used to determine ssDNA concentrations from fluorescence intensities.

5 Results and discussion

Thermal simulations

Given the relatively large volume capacity of a vacuum-driven chamber—typically an order of magnitude greater than that of conventional microfluidic systems—makes uniform heating for consistent reaction performance particularly challenging. Surface plasmonic heating *via* thin-film metals positioned at the chamber bottom is likely ineffective for such large volumes. In contrast, volumetric plasmonic heating *via* AuNRs throughout the chamber offers a more effective solution, enabling uniform thermal distribution. Fig. 2a illustrates this through simulated temperature profiles comparing these two heating approaches—volumetric heating *via* AuNRs and surface heating *via* thin-film Au—at the denaturation (90 °C) and annealing/extension (47 °C) stages. Along the chamber height, surface heating leads to a sharp temperature drop away from the heated bottom. In contrast, AuNR-based volumetric heating maintains a more consistent temperature, with a difference of 8.7 °C during denaturation and 2.4 °C during annealing/extension (Fig. 2b). Fig. 2c compares experimentally measured and simulated peak temperature profiles over time for a single thermal cycle. The deviation between experimental and simulated data remains within 3%. This close agreement validates the simulation model.

Thermal cycling characteristics

Fig. 3 illustrates the thermal cycling characteristics of bead-based plasmonic PCR under laser irradiation across various concentrations of AuNRs. In Fig. 3a, the temperature profiles over 20 amplification cycles are presented following an initial pre-heating step. Each cycle includes a denaturation phase at

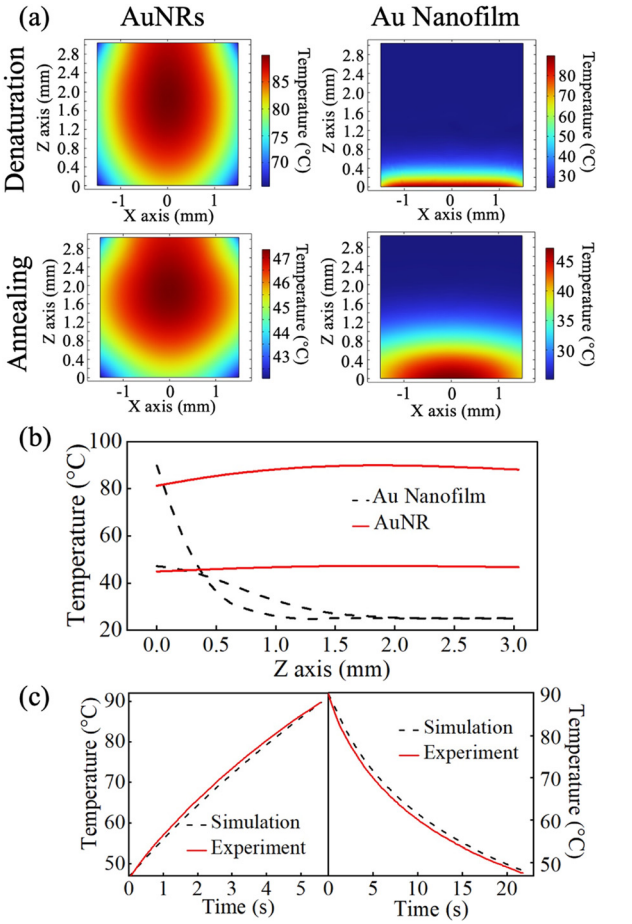

Fig. 2 Numerical simulation results. (a) Temperature distributions across the chamber plane along the axis of symmetry for two configurations: plasmonic heating *via* AuNRs dispersed within the chamber (left) and thin-film Au coating on the chamber bottom (right). Results are shown for a peak temperature of 90 °C (above) and 47 °C (below). (b) Corresponding temperature profiles along the axis of symmetry for each configuration. (c) Comparison between simulated and experimentally measured temperature profiles for plasmonic heating *via* AuNRs.

90 °C and an annealing/extension phase at an optimized temperature of 47 °C (Fig. S5). At a concentration of 0.5 nM AuNRs, the full set of 20 thermal cycles is completed in under 17 min. This duration drops below 12 min with the use of 2.5 nM AuNRs. However, further increasing the concentration to 9 nM yields only a marginal improvement, with the total cycling time approaching 10 min (Fig. 3b). This can be attributed to the influence of particle concentration on radiative transfer.[42] Increasing AuNR concentration beyond a certain point limits laser penetration into the bulk solution as most of the energy is absorbed or scattered near the illuminated surface. These results suggest that 2.5 nM AuNRs offer an optimal balance between performance and material efficiency, enabling rapid thermal cycling without excess material usage.

Heating and cooling rates are defined as the temperature change divided by the corresponding time interval during

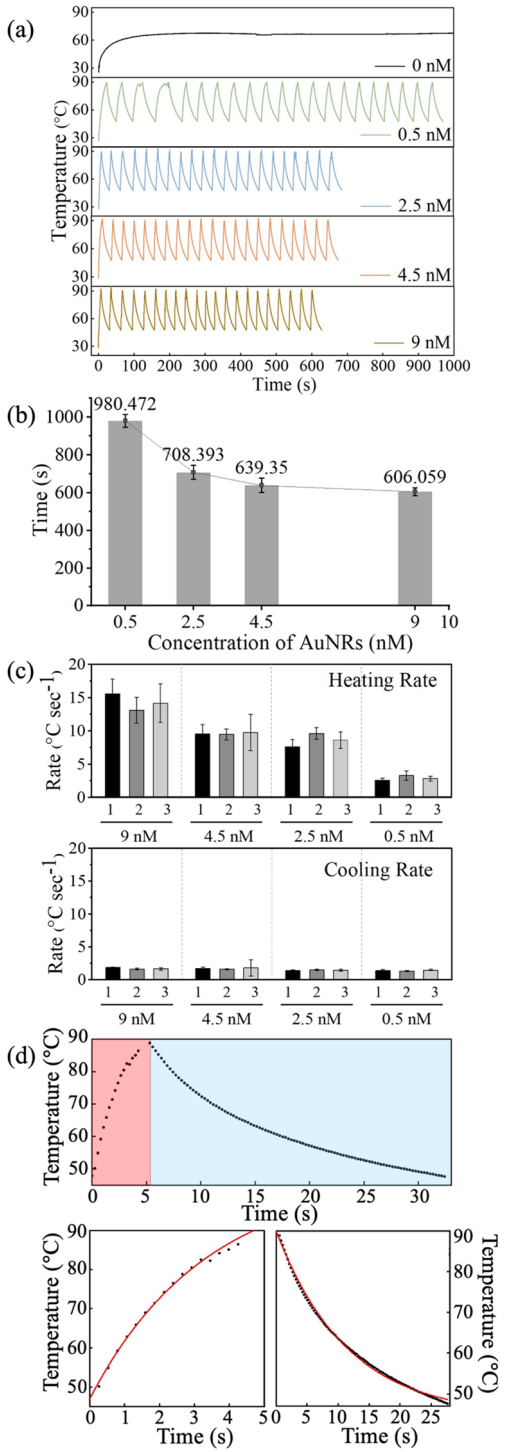

Fig. 3 Thermal cycling characteristics at different AuNR concentrations. (a) Temperature profiles over 20 cycles. (b) Total runtime values (n = 5). (c) Average heating and cooling rates (in triplicates). (d) Representative temperature profile over a cycle with 2.5 nM AuNRs along with the exponential fittings. The chamber contains a 21.5 μL PCR mixture with 60 μg magnetic beads and varying AuNR concentrations.

their respective phases. As shown in Fig. 3c, the average heating rate increases with AuNR concentration, peaking at 16 °C s^{-1} at 9 nM, whereas the cooling rate remains relatively constant at approximately 2 °C s^{-1} across all tested concentrations. The temperature profile for a single cycle at 2.5 nM AuNRs (Fig. 3d) reveals exponential heating and cooling behaviours, characterized by time constants of 3.4 s and 11.4 s, respectively. Furthermore, varying the bead amount, either by increasing to 90 μg or reducing to 10 μg, has a negligible impact on heating and cooling dynamics (Fig. S6), indicating robustness of the thermal cycling performance to bead quantity.

Impact of bead amount

Although bead amount has minimal impact on thermal cycling performance, it plays a critical role in PCR efficiency due to its function as a carrier for surface-bound primers. Insufficient bead amounts lead to low product yield while excessive amounts can also reduce yield primarily due to bead aggregation, which limits primer accessibility and may obstruct microchannels. Fig. 4a presents fluorescence microscopy images of representative beads used in varying amounts during a 20-cycle plasmonic PCR within the chamber followed by a purification wash. Strong fluorescence intensity indicates high accumulation of dsDNA amplicons on the bead surfaces. Fluorescence intensity increases with bead amount, peaking at 60 μg, after which a slight decline is observed (Fig. 4b). This peak corresponds to optimal availability of reverse primers while the subsequent drop is attributed to aggregation-induced

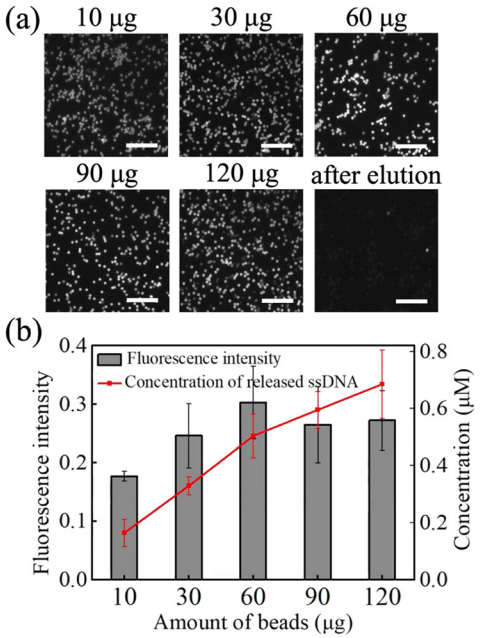

Fig. 4 Impact of bead amount on the results of 20-cycle PCR. (a) Fluorescence microscopy images (50×) of beads used in various amounts captured after a purification wash. Scale bars: 40 μm. (b) Normalized fluorescent intensity of the beads, quantified using ImageJ, plotted against bead amount, along with the concentration of eluted ssDNA in 6 μL of elution buffer, measured by UV-vis at 260 nm (n = 5). The chamber contains a 21.5 μL PCR mixture with 2.5 nM AuNRs irradiated by an 808-nm laser (0.28 W mm^{-2}).

reduction in accessible surface area, impairing annealing efficiency. Another contributing factor could be the bead and template imbalance; as bead amount increases without a rise in template concentration, fewer beads successfully capture and amplify template, resulting in diminished signal intensity. Despite this decrease in fluorescence beyond 60 μg, the concentration of ssDNA recovered after thermal elution continues to rise with bead amount (Fig. 4b). This trend is reasonable as a fixed elution volume (6 μL) extracts more ssDNA from a larger number of beads, even though individual beads contribute less indicated by reduced fluorescence.

Amplification efficiency

Amplification curves are commonly used to assess the target amplification efficiency. However, in this system, real-time fluorescence monitoring during thermal cycling is hindered by the background signal from fluorescently labelled forward primers, which are present in excess. This interference prevents accurate derivation of amplification curves from individual reactions. Reconstruction of these curves for each template concentration becomes feasible through repeat reactions, each involving a fresh batch of beads and a varied number of cycles, with bead fluorescence quantified post-purification following the final cycle, rather than monitored in real time. Fig. 5a displays reconstructed curves, each generated by fitting a sigmoid function to a data set corresponding to a specific template concentration, with bead fluorescence quantified following a purification wash. The cycle threshold (C_t) plot is shown in Fig. 5b, where C_t values are the cycle numbers at which fluorescence exceeds a baseline threshold of 0.063 (determined based on the background signal level observed in no-template controls). These values demonstrate a theoretically expected inverse linear relationship with the logarithm of the initial template concentration. A linear fitting yields a slope of −3.45 with an R^2 value of 0.949, indicating an amplification efficiency of 95%.

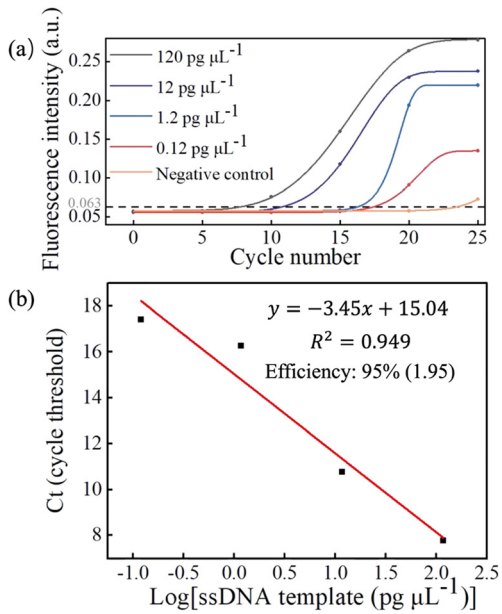

Fig. 5 (a) Amplification curves of template DNA at varying concentrations. (b) Standard curve plotting C_t values against logarithmic template concentrations.

ssDNA release and elution

ssDNA can be released after a purification step by denaturing surface-immobilized duplex accumulated on beads through either alkaline wash or heating. In this study, heat-based elution is applied, leveraging plasmonic heating, as alkaline conditions may promote biotin dissociation and unintended duplex release. Fig. 6a presents gel electrophoresis results of eluted products following thermal treatment at 40 °C, 60 °C, or 80 °C for 40 s. In all cases, a single band corresponding to 80-nt ssDNA appears, indicating that no detectable duplex was released. Furthermore, increasing the elution temperature enhances ssDNA recovery, likely due to more effective denaturation of duplexes at higher temperatures. Based on these findings, 80 °C was selected as the elution temperature for subsequent buffer comparison.

The choice of buffer can markedly influence both the efficiency of ssDNA elution and its compatibility with downstream use. Fig. 6b presents gel electrophoresis results of the eluted ssDNA under four different buffer conditions: ultrapure water, 10 mM Tris–HCl (pH = 8), 2.5 mM Tris–HCl (pH = 7.5), and TGK buffer. All four buffers yield single bands of similar intensity, corresponding to 80 nt ssDNA, indicating high purity and effective elution. These results confirm that each buffer is suitable for ssDNA recovery, with potential selection guided by downstream application.

ssDNA validation and recovery efficiency

It is essential to confirm that eluted products are indeed ssDNA, rather than duplexes, and to assess ssDNA recovery efficiency. Fig. 7a shows fluorescent intensity measurements from bead-

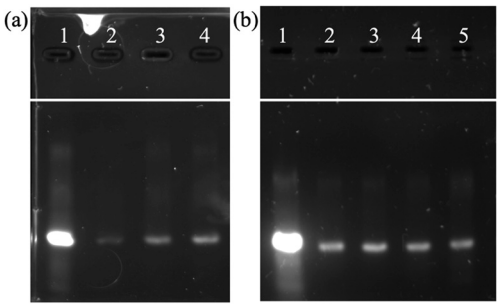

Fig. 6 Gel electrophoresis analysis of ssDNA eluted from beads following thermal denaturation (40 s) under varying temperature and buffer conditions. Lane 1 displays the 80 nt ssDNA template band used as a reference. (a) Elution at different temperatures using 10 mM Tris–HCl (pH 8.0) as the buffer. Lane 2: 40 °C; lane 3: 60 °C; and lane 4: 80 °C. (b) Elution at 80 °C using different buffers. Lane 2: ultrapure water; lane 3: 2.5 mM Tris–HCl (pH 7.5); lane 4: 10 mM Tris–HCl (pH 8.0); and lane 5: TGK buffer.

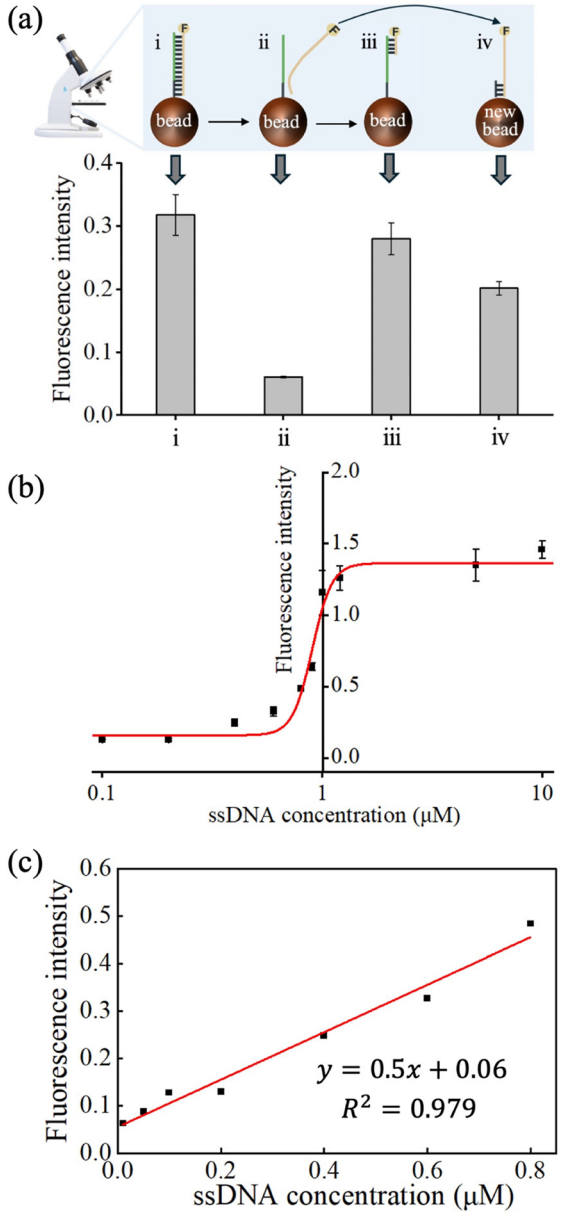

Fig. 7 ssDNA throughput and recovery. (a) Fluorescence intensity measurements from bead-bound DNA across four conditions: post-PCR beads before elution (i), after thermal elution (ii) followed by incubation with fluorescence-labelled forward primers (iii), and fresh reverse-primer beads incubated with collected elution products (iv). (b) Calibration curve generated from reverse-primer beads incubated with known ssDNA concentrations. (c) Dynamic region of the calibration curve with linear fitting used to determine the concentration of ssDNA corresponding to the measured fluorescence intensities from beads.

bound DNA. A comparison between post-PCR beads (20 thermal cycles) before (i) and after elution (ii) following a 40 s thermal treatment at 80 °C reveals a substantial decrease in fluorescence, indicating effective release of labelled strands. Subsequent incubation of the same beads with labeled forward primers yields a fluorescence increase to a level (iii) that nearly matches the original intensity, suggesting that complementary strands remain bead-bound and that the eluted products are predominantly ssDNA. This conclusion is further supported by observed fluorescence from a fresh batch of reverse-primer beads incubated with the eluted products for 12 h (iv). The slightly reduced signal is likely attributable to partial loss of ssDNA during the collection process.

ssDNA throughput can be estimated using a plot derived from fluorescence measurements of reverse-primer beads incubated with known concentrations of ssDNA (Fig. 7b). According to the dynamic region of this calibration curve (Fig. 7c), post-PCR beads (i) contain approximately 0.47 μM of ssDNA while the fresh beads incubated with eluted products (iv) exhibit a concentration of 0.31 μM, corresponding to a recovery efficiency of 66%. This is a conservative estimate, as it assumes complete hybridization of the eluted ssDNA to reverse primers, and comparable or even exceeds previously reported yields.[43,44] Additionally, the fluorescence from forward-primer incubation (iii) corresponds to a concentration of 0.43 μM, representing the amount of complementary strand retained on the beads. This indicates a retention rate of at least 92% and confirms that streptavidin remains stably immobilized on the bead surface following thermal elution. Our ssDNA recovery efficiency and yield are comparable or exceed those of existing methods, with a total processing time of less than 15 min—significantly faster than conventional approaches that typically require several hours (Table S3).

Automated microfluidic workflow

The automated microfluidic workflow (SI Movie) proceeds through five sequential stages: (1) loading the PCR chamber; (2) removing post-PCR waste; (3) performing a purification wash; (4) introducing the elution buffer; and (5) executing elution following thermal release. These operations are coordinated *via* specific valve activation and application of vacuum to designated chambers (Fig. S7). Accurate liquid handling is achieved through calibrated valve actuation. The correlation between valve-opening duration and dispensed volume remains stable, allowing precise control of master mix (11.5 μL), ssDNA template (5 μL), magnetic beads (5 μL, 60 μg), and elution buffer (6 μL). Measured residual volumes confirm that the transported volumes match the intended inputs. Fabrication-specific factors—such as channel geometry and layer stiffness—may influence valve performance but these are readily corrected through calibration. Fig. S8a shows the dispensed volume as a function of valve-opening duration for microvalve V3, with vacuum applied to the PCR chamber. It follows a linear trend (R^2 = 0.998) for valve-opening durations between 150 and 400 ms and remains consistent over repeated use. Volume variations fall below 6% after 1000 actuation cycles, except at durations shorter than 100 ms (Fig. S8b), likely due to unsteady flow during brief actuation. Importantly, the valve exhibits no signs of physical damage or delamination following the cycling test (Fig. S8c). These results are representative of the remaining microvalves in the system.

Vacuum-driven chambers are central to the workflow. Unlike conventional shallow chambers, these chambers are

up to two orders of magnitude deeper, enabling large volume handling with microfluidic precision. The cylindrical chamber, with a radius of 1.5 mm and a height of 7 mm, has a capacity of approximately 50 μL. To ensure adequate headspace and prevent overflow, the chamber is typically filled with up to 40 μL of solution. However, to minimize the risk of unintended aspiration during vacuum activation, experiments here employed only ~22 μL—roughly half of the available capacity. Scaling to larger volumes is feasible by increasing the chamber diameter and pneumatic layer thickness, though this may extend thermal cycling times due to increased thermal mass. The system has been validated for up to 40 PCR cycles, which is typically sufficient for applications. Beyond this, nonspecific amplification and byproduct formation may increase, potentially compromising yield and specificity.

This multiscale architecture challenges pressure-driven flow with incomplete fluid exchange, primarily flushing the lower chamber leaving rest under-washed (Fig. S9a). Direct vacuum access to these chambers allows complete filling whereas conventional pressure-driven flow without such access fills only a small portion (Fig. S9b). Likewise, it enables near complete fluid removal (90%) without loss to branching channels even in the absence of microvalves, thereby simplifying overall design (Fig. S9c). Moreover, vacuum-driven chambers can be also advantageous for routing fluids through select branches within complex channel networks using fewer microvalves. Additionally, they mitigate leakage concerns as they tolerate variations in interlayer bonding strength. Performing PCR in vacuum-driven chambers offers practical advantages. Despite the lack of oil encapsulation, evaporation is tolerable due to relatively large reaction volume, resulting in an average loss of only 14% over 20 thermal cycles (n = 10). This limited evaporation is mainly attributed to rapid thermocycling, which minimizes dwell time at the denaturation temperature, and to the quick saturation of the small headspace with vapor. Lastly, the absence of bubbles during thermocycling—a common issue encountered in chip-based PCR—can be attributed to their buoyant escape into the air pocket in the chamber's upper zone.

6 Conclusions

We have demonstrated a multiscale microfluidic platform that bridges the gap between high-volume fluid processing and microfluidic precision. Using multilayer soft lithography, we integrated vacuum-driven deep chambers into microfluidics, enabling automated processing of reaction volumes beyond the limits of conventional microfluidics. This automated platform was applied to the rapid high-volume generation of ssDNA. Strand-selective amplification and separation were achieved *via* bead-based PCR while fast thermocycling of large volumes was enabled by volumetric heating owing to plasmonic AuNRs dispersed in the reaction mixture. Thermal elution (also *via* plasmonic heating) from the beads facilitated efficient strand release with minimal contamination by dsDNA. This work lays the foundation for future high-volume microfluidics, expanding the lab-on-a-chip technologies beyond analytical applications. In addition to ssDNA generation, the platform can be extended to other important applications such as protein purification,[45] enrichment and purification of rare cells and exosomes,[46,47] and detection of pathogens.[48] Integration with an upstream separation module is currently underway to fully automate the SELEX process.

Author contributions

Conceptualization, L. Y., Y. B. and A. H. Methodology, L. Y., Y. B., A. H., Y. L., S. N. and Y. C. L. Validation, A. H., Y. B., Y. L., S. N. and Y. C. L. Formal analysis, A. H. Writing – original draft, review & editing, L. Y. and A. H. Supervision, Resources, Project administration and Funding acquisition, L. Y.

Conflicts of interest

There are no conflicts to declare.

Data availability

The data supporting this article have been included as part of the supplementary information (SI).

Supplementary information: simulations, supplementary figures and tables as well as a supplementary movie. See DOI: **https://doi.org/10.1039/d5lc00785b**.

Acknowledgements

This project was financially supported by the Innovation and Technology Support Programme (ITSP) of the Hong Kong Innovation and Technology Fund (Project No. ITS/048/22), with industrial contribution from Immuno Cure Holding (HK) Limited. We acknowledge the Nanosystem Fabrication Facility (CWB, HKUST) for assistance with microfabrication.

Notes and references

1 M. Ronaghi, M. Uhlén and P. Nyrén, *Science*, 1998, **281**, 363.
2 T. Hultman, S. Stahl, E. Homes and M. Uhlen, *Nucleic Acids Res.*, 1989, **17**, 4937.
3 F. Erdogan, R. Kirchner, W. Mann, H. H. Ropers and U. A. Nuber, *Nucleic Acids Res.*, 2001, **29**, e36.
4 P. C. Kao, S. T. Ding, E. C. Lin, K. C. Li, L. Wang and Y. W. Lu, *Microfluid. Nanofluid.*, 2014, **17**, 477.
5 M. Orita, H. Iwahana, H. Kanazawa, K. Hayashi and T. Sekiya, *Proc. Natl. Acad. Sci. U. S. A.*, 1989, **86**, 2766.
6 F. A. Ran, P. D. Hsu, J. Wright, V. Agarwala, D. A. Scott and F. Zhang, *Nat. Protoc.*, 2013, **8**, 2281.
7 K. Tang, D. J. Fu, D. Julien, A. Braun, C. R. Cantor and H. Köster, *Proc. Natl. Acad. Sci. U. S. A.*, 1999, **96**, 10016.
8 D. J. Lockhart, H. Dong, M. C. Byrne, M. T. Follettie, M. V. Gallo and M. S. Chee, *et al.*, *Nat. Biotechnol.*, 1996, **14**, 1675.
9 M. Schena, D. Shalon, R. W. Davis and P. O. Brown, *Science*, 1995, **270**, 467.

10 M. Alafeef, K. Dighe, P. Moitra and D. Pan, *ACS Nano*, 2020, **14**, 17028.
11 M. Liss, B. Petersen, H. Wolf and E. Prohaska, *Anal. Chem.*, 2002, **74**, 4488.
12 L. L. Li, P. Ge, P. R. Selvin and Y. Lu, *Anal. Chem.*, 2012, **84**, 7852.
13 H. Y. Ko, J. H. Lee, H. Kang, S. H. Ryu, I. C. Song and D. S. Lee, *et al.*, *J. Nucl. Med.*, 2010, **51**, 98.
14 K. Abnous, N. M. Danesh, M. Ramezani, M. Alibolandi, M. A. Nameghi and T. S. Zavvar, *et al.*, *Anal. Chim. Acta*, 2021, **1165**, 338549.
15 M. Zhang, B. Huo, S. Yuan, B. Ning, J. Bai and Y. Peng, *et al.*, *Anal. Chim. Acta*, 2018, **1043**, 98.
16 Y. Seetang-Nun, W. Jaroenram, S. Sriurairatana, R. Suebsing and W. Kiatpathomchai, *Mol. Cell. Probes*, 2013, **27**, 71.
17 S. Khunthong, W. Jaroenram, N. Arunrut, R. Suebsing, I. Mungsantisuk and W. Kiatpathomchai, *J. Virol. Methods*, 2013, **188**, 51.
18 D. Pinkel, T. Straume and J. W. Gray, *Proc. Natl. Acad. Sci. U. S. A.*, 1986, **83**, 2934.
19 H. Daims, A. Brühl, R. Amann, K. H. Schleifer and M. Wagner, *Syst. Appl. Microbiol.*, 1999, **22**, 434.
20 C. Tuerk and L. Gold, *Science*, 1990, **249**, 505.
21 Y. Jiang, M. Shi, Y. Liu, S. Wan, C. Cui, L. Zhang and W. Tan, *Angew. Chem., Int. Ed.*, 2017, **56**, 11916.
22 S. He, F. Gao, J. Ma, H. Ma, G. Dong and C. Sheng, *Angew. Chem.*, 2021, **133**, 23487.
23 G. Zu, Y. Cao, J. Dong, Q. Zhou, P. Van Rijn, M. Liu and R. Pei, *ACS Appl. Bio Mater.*, 2018, **2**, 406.
24 D. Dell'Atti, M. Zavaglia, S. Tombelli, G. Bertacca, A. O. Cavazzana and G. Bevilacqua, *et al.*, *Clin. Chim. Acta*, 2007, **383**, 140.
25 S. T. Lovett and R. D. Kolodner, *Proc. Natl. Acad. Sci. U. S. A.*, 1989, **86**, 2627.
26 M. J. Kujau and S. Wölfl, *Mol. Biotechnol.*, 1997, **7**, 333.
27 T. Hultman, S. Stahl, E. Homes and M. Uhlen, *Nucleic Acids Res.*, 1989, **17**, 4937.
28 N. C. Pagratis, *Nucleic Acids Res.*, 1996, **24**, 3645.
29 U. B. Gyllensten and H. A. Erlich, *Proc. Natl. Acad. Sci. U. S. A.*, 1988, **85**, 7652.
30 J. A. Sanchez, K. E. Pierce, J. E. Rice and L. J. Wangh, *Proc. Natl. Acad. Sci. U. S. A.*, 2004, **101**, 1933.
31 K. E. Pierce, J. A. Sanchez, J. E. Rice and L. J. Wangh, *Proc. Natl. Acad. Sci. U. S. A.*, 2005, **102**, 8609.
32 J. Shendure, G. J. Porreca, N. B. Reppas, X. Lin, J. P. McCutcheon and A. M. Rosenbaum, *et al.*, *Science*, 2005, **309**, 1728.
33 C. R. McEvoy, T. Semple, B. Yellapu, D. Y. Choong, H. Xu and G. Mir Arnau, *et al.*, *BioTechniques*, 2020, **68**, 48.
34 A. Lermo, S. Campoy, J. Barbe, S. Hernández, S. Alegret and M. I. Pividori, *Biosens. Bioelectron.*, 2007, **22**, 2010.
35 J. P. Hilton, T. Nguyen, M. Barbu, R. Pei, M. Stojanovic and Q. Lin, *Microfluid. Nanofluid.*, 2012, **13**, 749.
36 T. Kojima, Y. Takei, M. Ohtsuka, Y. Kawarasaki, T. Yamane and H. Nakano, *Nucleic Acids Res.*, 2005, **33**, e150.
37 P. J. Roche, L. K. Beitel, R. Khan, R. Lumbroso, M. Najih and M. C. K. Cheung, *et al.*, *Analyst*, 2012, **137**, 4475.
38 A. Jalili, M. Bagheri, A. Shamloo and A. H. Kazemipour Ashkezari, *Sci. Rep.*, 2021, **11**, 23338.
39 S. M. Meyer, J. Pettine, D. J. Nesbitt and C. J. Murphy, *J. Phys. Chem. C*, 2021, **125**, 16268.
40 V. P. Pattani and J. W. Tunnell, *Lasers Surg. Med.*, 2012, **44**, 675.
41 P. J. Roche, M. Najih, S. S. Lee, L. K. Beitel, M. L. Carnevale and M. Paliouras, *et al.*, *Analyst*, 2017, **142**, 1746.
42 W. An, Q. Zhu, T. Zhu and N. Gao, *Exp. Therm. Fluid Sci.*, 2013, **44**, 409.
43 L. Civit, A. Fragoso and C. K. O'Sullivan, *Anal. Biochem.*, 2012, **431**, 132.
44 M. Avci-Adali, A. Paul, N. Wilhelm, G. Ziemer and H. P. Wendel, *Molecules*, 2009, **15**, 1.
45 C. Schmidli, S. Albiez, L. Rima, R. Righetto, I. Mohammed and P. Oliva, *et al.*, *Proc. Natl. Acad. Sci. U. S. A.*, 2019, **116**, 15007.
46 A. A. Kajani, L. Rafiee, M. Samandari, M. A. Mehrgardi, B. Zarrin and S. H. Javanmard, *RSC Adv.*, 2022, **12**, 32834.
47 A. Meggiolaro, V. Moccia, A. Sammarco, P. Brun, C. C. Damanti and B. Crestani, *et al.*, *Sens. Actuators, B*, 2024, **409**, 135583.
48 Y. Kim, A. T. Abafogi, B. M. Tran, J. Kim, J. Lee and Z. Chen, *et al.*, *Micromachines*, 2020, **11**, 203.

